Antarctic sea ice expansion and Southern Ocean cooling linked to tropical internal variability

Eui-Seok Chung[1], Seong-Joong Kim[1*], Axel Timmermann[2,3], Kyung-Ja Ha[2,4,5], Sang-Ki Lee[6], Malte F. Stuecker[7], Keith B. Rodgers[2,3], Sun-Seon Lee[2,3], and Lei Huang[2,3]

[1]Division of Atmospheric Sciences, Korea Polar Research Institute, Incheon, South Korea
[2]Center for Climate Physics, Institute for Basic Science, Busan, South Korea
[3]Pusan National University, Busan, South Korea
[4]Department of Climate System, Pusan National University, Busan, South Korea
[5]

[6]Atlantic Oceanographic and Meteorological Laboratory, NOAA, Miami, FL, USA
[7]Department of Oceanography and International Pacific Research Center, School of Ocean and Earth Science and Technology, University of Hawai‘i at Mānoa, Honolulu, HI, USA

*e-mail: seongjkim@kopri.re.kr

Abstract

A variety of hypotheses for explaining the observed Antarctic sea ice expansion over the period of continuous satellite monitoring and corresponding model-observation discrepancy have been proposed, but the issue remains unresolved. Here, by comparing multiple Large Ensembles of model simulations with available observations, we show that Antarctic sea ice has expanded due to ocean surface cooling associated with multi-decadal variability in the Southern Ocean that temporarily outweighs the opposing forced response, along with sub-iceshelf melting and stratospheric ozone depletion. In both observations and model simulations, the multi-decadal variability in the Southern Ocean is closely linked to internal variability in the tropics, especially in the Pacific, via atmospheric teleconnections. The linkages are, however, distinctly weaker in simulations than in observations, accompanied by a distinctly stronger global-mean warming response in simulations resulting from model biases and weaker tropical internal variability. Thus, the forced response dominates in simulations, resulting in apparent model-observation discrepancy.

Introduction

Continuous satellite observations since ~1979 indicate a pronounced interhemispheric asymmetry in sea ice change, with a modest expansion in the Southern Ocean (SO) despite the global warming trend[1,2]. Unlike the marked sea ice decline in the Arctic, the Antarctic sea ice expansion, which is accompanied by an overall cooling of sea surface temperature (SST) in the SO[3–6], has not been reproduced by climate models over 1979–2014, under historical forcing[7–12]. Considering that Antarctic sea ice changes affect ocean-atmosphere heat and momentum exchanges, ocean carbon uptake, ecosystems, and the thermohaline circulation[13], this marked discrepancy may have serious implications for the credibility of near-term model-projected climate change.

It has been suggested that Antarctic sea ice expansion has been due to increased freshwater fluxes[14–21] and changes in the Southern Annular Mode and associated SO circulation changes[5,22–27], with this triggered by increased greenhouse gas concentrations and human-induced stratospheric ozone depletion. Although model deficiencies in representing these mechanisms cannot be ruled out[8,9,28,29], several other studies have suggested that the Antarctic sea ice expansion may have arisen from internal climate variability[3,4,7,9,11,30,31], with this tied in part to climate variability in the Pacific and Atlantic Oceans[12,32–40]. The recent multi-year Antarctic sea ice decline[2,8,36,41–43] seems to fit into this view. However, both the main cause of the satellite-observed sea ice expansion, whether external forcing or internal variability, and the question of why models fail to reproduce observations under historical forcing, remains unresolved[13,16,17,44–47]. Based on the fact that regional patterns of sea ice trends are mainly governed by wind fields[48], ref. 26 demonstrated that applying realistic wind forcing along with realistic SSTs is essential for reproducing the observations. This implies that climate models may have deficiencies in representing teleconnection processes that affect SO wind and SST fields.

One of the major obstacles to resolving these issues is the inherent difficulty in separating the observed changes over the relatively short historical period (i.e., 1979–2014) into externally forced changes and internal variability. As the influence of internal variability on long-term trends diminishes with increasing time span[49] (Supplementary Text 1), we employ a long-term SST record in the SO (1950–2020) as a proxy for Antarctic sea ice. Here, using the long-term proxy record and large-ensemble climate model simulations, we attempt to elucidate the main processes responsible for the satellite-observed sea ice expansion and the causes of the model-observation discrepancy.

Results

Sea Ice and SST Changes in the Southern Ocean

Before delving into the causes of the observed sea ice expansion, we examine annual-mean total sea ice extent (SIE) and SO (south of 50°S) SST trends over 1979–2014, for which continuous satellite observations are available and each of the models analyzed in this study is represented by more than 15 ensemble members (Methods). The satellite observations indicate a statistically significant sea ice expansion at a rate of $0.223\pm0.087\times10^6$ km^2 $decade^{-1}$ over this period (Fig. 1a, solid line in red), which is not captured by the model simulations analyzed in this study (dark blue boxes tagged as Hist in Fig. 1a). A marked model-observation discrepancy is also apparent over periods other than 1979–2014, but this discrepancy doesn't appear to grow further with increases in time span (Fig. 2a). Moreover, the observed SIE trend over 1979–2020 is not statistically significant, raising a question about the argument that the sign of model-simulated forced response is incorrect.

The satellite-observed Antarctic sea ice expansion over 1979–2014 results from large increases in the Indian and West Pacific sectors, especially in the Ross Sea, despite moderate decreases in the Amundsen and Bellingshausen Seas (Fig. 3a). As noted in previous studies[3,4,6], the overall expansion of Antarctic sea ice occurred along with surface cooling in the SO (red lines in Fig. 1b), particularly in the Pacific sector (Fig. 3b). In contrast, the model-simulated forced response exhibits spatially coherent sea ice decline (Fig. 3c) and ocean surface warming (Fig. 3d) over the same period, which is consistent with increasing global temperatures, although inter-model spread is substantial. Note that all models analyzed in this study fail to capture the observed SIE/SST trends (dark blue boxes tagged as Hist in Extended Data Figs. 1a and 1d).

To determine whether the model-observation discrepancy arises from an insufficient number of ensemble members or from external forcing, model-simulated trends under pre-industrial conditions are computed from all possible overlapping 36-year segments of corresponding pre-industrial control runs (dark blue boxes tagged as PI in Figs. 1a and 1b and Extended Data Figs. 1b and 1e). The observed SIE/SST trends over 1979–2014 lie within the range simulated by climate models in the absence of external forcings, in line with previous studies suggesting that the observed sea ice expansion can be accounted for by internal variability alone[9,23]. Next, assuming that internal variability is state-independent, the distribution in the PI case is adjusted by adding the ensemble-mean trend (Supplementary Table 2), which can be regarded as externally forced response, for each model over 1979–2014 (dark blue boxes tagged as PI + Forced in Figs. 1a and 1b and Extended Data Figs. 1c and 1f). Note that adding the forced response causes most climate models to fail in capturing the observed trends (Extended Data Figs. 1c and 1f). These results imply that the model-observation discrepancy stems from either an overestimated forced response or underestimated internal variability in model simulations, rather than insufficient ensemble size.

The potential overestimation of model-simulated SIE decrease can arise from not only missing freshwater forcing in simulations[21], but also model biases in the global-mean warming response[9,28]. Scatterplots of the SIE trends with corresponding global-mean warming trends over 1979–2014 (Fig. 2b) and 1979–2020 (Fig. 2c) suggest that as noted in ref. 9, the global-mean warming response is distinctly stronger in model simulations and thereby contributes to the model-observation discrepancy in SIE trends. The mismatch in the global-mean warming response appears to stem primarily from biases in model climate sensitivity[9], but part of the mismatch may arise due to internal variability. For instance, the time evolution of the CESM2 ensemble-mean, annual-mean global-mean surface temperature anomaly over 1950–2020, which can be regarded as a forced response, agrees well with observations (Extended Data Fig. 2a). However, the difference between observations and the CESM2 ensemble mean, which can be regarded as internal variability, exhibits a strong negative trend over 1979–2014 (Extended Data Fig. 2b), implying that the apparent model-observation discrepancy in the Antarctic SIE trend can be caused by internal variability through a mismatch in global-mean warming trends. In fact, pacemaker experiments (Methods), in which observed SST anomalies in the eastern equatorial Pacific were assimilated, demonstrate that this negative trend can be driven by SST variability in the eastern equatorial Pacific (Extended Data Fig. 2c), in agreement with previous studies[50]. These results therefore suggest that the model-observation mismatches in both SIE and global-mean warming responses can be attributed in part to tropical internal variability.

To determine whether the observed SIE expansion over 1979–2014 can be explained by internal variability, the time evolution of the annual-mean SIE anomaly in the observations with respect to the 1979–2020 climatology is compared with the model simulations (Fig. 1c). While the ensemble-mean changes exhibit a largely monotonic decline over time (solid lines in color other than red), the observations (red lines) suggest a substantial multi-decadal variability[3,4,7] over 1964–2020. According to the NSIDC G02135 data (solid line in red), the observed expansion over 1979–2014 was virtually cancelled out by a precipitous decline over the subsequent years and since then has returned to mean values for the satellite record[2,8,9,41,43]. Furthermore, the NSIDC-0192 (dashed line in red) and G00917 (dash-dotted line in red) data indicate that the observed expansion over 1979–2014 was preceded by a marked decline in the 1970s. As noted in ref. 7, the Nimbus-1 SIE anomaly for September 1964 (red dot) further suggests that the observed expansion over 1979–2014 was driven by internal variability. Although the observed short-term trends are not always in agreement with model simulations, the sign of the observed changes over 1964–2020 is broadly consistent with the models' forced response.

Due to the absence of continuous satellite observations before 1979, it is not possible to quantify sea ice changes over the entire 70-year period. However, considering the close relationship between SIE and SST changes, comparisons of SST observations with the model's forced response can shed light on observed sea ice changes. The sign of the observed long-term SST changes over the entire 70-year period largely agrees with the model's forced response (Fig. 1d). As shown in ref. 3, a strong contrast in the sign of observed SST trends is found between 1950–1978 (orange lines, warming) and 1979–2014 (red lines, cooling) in Fig. 1b, with the positive trends in the former period implying overall Antarctic sea ice reduction, as in the model simulations (yellow green boxes tagged as Hist in Fig. 1a and Extended Data Fig. 1a). In contrast, model simulations consistently exhibit SST increases, with the latter period showing a substantially enhanced warming (Extended Data Figs. 1d and 1f). Interestingly, the observed SST warming over 1950–1978 is noticeably stronger than the model's forced response, implying that the influence of internal variability and greenhouse gas forcing on SSTs acted in the same direction. These characteristics provide further support for the argument emphasizing a role for internal variability.

Connections with Tropical Internal Variability

The overall expansion of Antarctic sea ice and concurrent ocean surface cooling in the SO over 1979–2014 was accompanied by distinct cooling in the central-to-eastern tropical Pacific and pronounced warming in the Northwest/Southwest Pacific and the North Atlantic (Figs. 3a and 3b). This implies the potential linkages between the observed changes in the SO and the Interdecadal Pacific Oscillation (IPO, Methods) and Atlantic Multidecadal Variability (AMV, Methods), as suggested by previous studies[32–40] and discussed in depth in ref. 51. We examine whether the unforced components of SO sea ice and SST changes are linked primarily to the IPO and AMV.

Assuming that the linear trends of SST over 1950–2020 represent the forced response, internal variability is estimated at each grid point through linear detrending. The detrended timeseries of the observed SO-mean SST anomaly indicate the presence of multi-decadal variability (red lines in Fig. 4a) along with strong negative trends over 1979–2014, which appear to be closely linked to markedly reduced global-mean warming response over the same period (Extended Data Fig. 2). The correlation between the detrended SST timeseries at each grid point and the corresponding SO-mean timeseries over 1950–2020 confirms the connection of the SO SSTs to both the IPO and AMV (Fig. 4b). The spatial patterns of regression slope against the AMV (Extended Data Fig. 3a) and IPO (Extended Data Fig. 3b) indices further highlight these connections, which are also evident in other reconstructed/reanalysis datasets (Extended Data Fig. 4). The Pacific sector is mainly linked to the IPO during all seasons, while the Atlantic sector appears to have been more sensitive to the AMV, especially, in austral summer and fall (Extended Data Fig. 5).

The forced response is unlikely to be linear over time, in particular for SIE[52]. Thus we also identify the internal variability component by subtracting off, for each grid point and year, the simulated ensemble-mean of annual-mean SST anomalies over 1950–2020. Despite inter-model discrepancies in the forced response, especially anthropogenic aerosol-cloud interactions[53], the resulting unforced component of SST changes in the SO is highly correlated with both IPO and AMV (Extended Data Figs. 3c-h).

To examine whether similar relationships hold in climate models, regression coefficients of SST and sea ice concentration changes against the AMV and IPO indices are computed for each model using their pre-industrial control run output. The regression slopes against the AMV index exhibit a substantial inter-model discrepancy in terms of spatial patterns and sign (Extended Data Figs. 6 and 7, left panels), implying that the AMV signal may not be robust in Antarctic sea ice[10]. In contrast, all models reasonably depict the connection of SST and sea ice concentration in the Pacific sector to the IPO[10,12,36,37] (Extended Data Figs. 6 and 7, right panels). However, unlike in the observations (Extended Data Fig. 3b), the IPO regression coefficients over the Pacific sector of the SO are noticeably smaller than those over the central-to-eastern tropical Pacific in the simulations (Extended Data Fig. 6, right panels). Moreover, the IPO tends to exert a weaker influence over the SO, particularly over the eastern Pacific sector, in the simulations. To assess these discrepancies more quantitatively, SST trends congruent with the observed IPO and AMV trends over 1979–2014 (Methods) are computed using the multiple linear regression coefficients from both observations and model simulations under pre-industrial conditions (Figs. 4c and 4d). Cooling is pronounced in the Pacific sector of the SO for both observations and simulations, but the IPO and AMV-induced SO-mean cooling is distinctly weaker (~70%) in the simulations with large inter-model spread (Extended Data Fig. 8). A similar model-observation discrepancy is found in the congruent sea ice concentration trends (Extended Data Fig. 9). These discrepancies imply potential model deficiencies in representing IPO/AMV-linked teleconnection processes.

Given that this period coincides with the AMV and IPO phase transitions (Fig. 4a), despite potential model deficiencies, we further investigate whether the AMV and IPO phase transitions can explain part of the observed changes using output from idealized coupled-model SST forcing experiments (Methods). In agreement with previous work on how the AMV and IPO are linked to Antarctic sea ice changes[36,37,39,40], a negative-to-positive phase transition of the AMV leads to modest sea ice expansion and surface cooling in the West Pacific sector, while sea ice decline and surface ocean warming in the Amundsen and Bellingshausen Seas is associated with an intensification of the Amundsen Sea Low (Fig. 5a-c). We note, however, that these AMV-induced changes are not robust. Although the spatial pattern is noticeably different from observations, a positive-to-negative phase transition of the IPO results in an overall sea ice expansion and surface cooling and a marked deepening of the Amundsen Sea Low (Fig. 5d-f), which has been linked to atmospheric Rossby waves emanating from the tropical Pacific[32,35–38]. In addition, a strengthening of westerlies at ~60°S and related enhanced northward Ekman transport (Fig. 5f) are likely to facilitate sea ice expansion during cold seasons[54].

To further illustrate that internal climate variability is responsible, in part, for the opposing SST/SIE trends between 1950−1978 and 1979−2014, we also analyzed coupled-model pacemaker experiments. Although year-to-year fluctuations are substantial and the long-term trend is weak (and the impact of equatorial Pacific SSTs on Antarctic sea ice trends could be model-dependent[27]), these model simulations broadly reproduce the opposing SST/SIE trends between the two periods (Fig. 4a and Extended Data Fig. 10).

Summary and Discussion

In this study, we provide compelling evidence that the observed Antarctic sea ice expansion over 1979−2014 occurred, in large part, as a result of internal variability, linked to the IPO and/or AMV, overpowering temporarily the forced response. In contrast, tropical teleconnections to the SO are distinctly weaker, in general, in model simulations. We also emphasize that part of the model-observation mismatch in global-mean warming response is attributable to tropical internal variability[50]. This implies that skillful near-term decadal prediction of Antarctic sea ice change should, to some degree, be contingent upon improving the representation of processes controlling internal variability[26]. Since model biases in ocean stratification and westerlies, among many others, can affect both internal variability and forced response, correcting such biases is a pre-requisite for improving internal variability processes.

The phase of IPO shifted from negative to positive around 2015. If the IPO were truly one of the major factors governing Antarctic sea ice variability, one would expect that the IPO-induced SIE change over recent years is in the opposite direction to what it was over 1979–2014. Consistent with this conjecture, recent years have witnessed a rapid decline of Antarctic sea ice (Fig. 1c), and modeling studies have demonstrated that the recent turnaround is linked in part to the IPO phase shift[36,42].

The failure of models to reproduce the observed Antarctic sea ice expansion is attributed, in large part, to weaker reproduction of large multi-decadal internal variability in the SO. However, given model biases (including stronger global warming[9]) and model deficiencies, one should not infer that the observed sea ice expansion can be explained exclusively by IPO/AMV-linked teleconnections because other factors such as increased freshwater fluxes[14–21] and stratospheric ozone depletion[22] might also play important roles. In particular, the model-observation discrepancy could be caused entirely by missing freshwater fluxes in model simulations. However, the associated uncertainties are enormous due to the absence of continuous long-term observations of sub-iceshelf melting and the phasing of freshwater fluxes. Moreover, the Antarctic sea ice response to freshwater forcing is highly sensitive to models and implementation method, as reflected in a pronounced inconsistency among previous modeling studies[14–21]. Given strong seasonality and regional differences in the Antarctic sea ice trend[36,54], further investigation is required to fully understand Antarctic sea ice changes and variability by accounting for all these processes together, which will be contingent on sustaining a multi-decadal multi-platform observing system and resolving existing issues in model simulations.

References

1. Turner, J., Hosking, J. S., Bracegirdle, T. J., Marshall, G. J. & Phillips, T. Recent changes in Antarctic sea ice. *Phil. Trans. R. Soc. A* **373**(2045), 20140163 (2015).
2. Parkinson, C. L. A 40-y record reveals gradual Antarctic sea ice increases followed by decreases at rates far exceeding the rates seen in the Arctic. *Proc. Natl Acad. Sci. USA* **116**(29), 14,414–14,423 (2019).
3. Fan, T., Deser, C. & Schneider, D. P. Recent Antarctic sea ice trends in the context of Southern Ocean surface climate variations since 1950. *Geophys. Res. Lett.* **41**(7), 2419–2426 (2014).
4. Armour, K. C. & Bitz, C. M. Observed and projected trends in Antarctic sea ice. *US CLIVAR Variations* **13**(4), 12–19 (2015).
5. Armour, K. C., Marshall, J., Scott, J. R., Donohoe, A. & Newsom, E. R. Southern Ocean warming delayed by circumpolar upwelling and equatorward transport. *Nat. Geosci.* **9**(7), 549–554 (2016).
6. Comiso, J. C. et al. Positive trend in the Antarctic sea ice cover and associated changes in surface temperature. *J. Clim.* **30**(6), 2251–2267 (2017).
7. Gagné, M.-É., Gillett, N. P. & Fyfe, J. C. Observed and simulated changes in Antarctic sea ice extent over the past 50 years. *Geophys. Res. Lett.* **42**(1), 90–95 (2015).

8. Chemke, R. & Polvani, L. M. Using multiple large ensembles to elucidate the discrepancy between the 1979-2019 modeled and observed Antarctic sea ice trends. *Geophys. Res. Lett.* **47**(15), e2020GL088339 (2020).
9. Roach, L. A. et al. Antarctic sea ice area in CMIP6. *Geophys. Res. Lett.* **47**(9), e2019GL086729 (2020).
10. Hobbs, W. R., Bindoff, N. L. & Raphael, M. N. New perspectives on observed and simulated Antarctic sea ice extent trends using optimal fingerprinting techniques. *J. Clim.* **28**(4), 1543–1560 (2015).
11. Jones, J. M. et al. Assessing recent trends in high-latitude Southern Hemisphere surface climate. *Nat. Clim. Change* **6**(10), 917–926 (2016).
12. Schneider, D. P. & Deser, C. Tropically driven and externally forced patterns of Antarctic sea ice change: reconciling observed and modeled trends. *Clim. Dynam.* **50**(11-12), 4599–4618 (2018).
13. IPCC. Climate change 2013: The physical science basis. In T. F. Stocker, et al. (Eds.), Contribution of Working Group I to the Fifth Assessment Report of the Intergovernmental Panel on Climate Change (p. 1535). Cambridge, United Kingdom and New York, NY, USA. Cambridge University Press (2013).
14. Menviel, L., Timmermann, A., Timm, O. E. & Mouchet, A. Climate and biogeochemical response to a rapid melting of the West Antarctic Ice Sheet during interglacials and implications for future climate. *Paleoceanography* **25**(4), PA4231 (2010).
15. Bintanja, R., van Oldenborgh, G. J., Drijfhout, S. S., Wouters, B. & Katsman, C. A. Important role for ocean warming and increased ice-shelf melt in Antarctic sea-ice expansion. *Nat. Geosci.* **6**(5), 376–379 (2013).

16. Swart, N. C. & Fyfe, J. C. The influence of recent Antarctic ice sheet retreat on simulated sea ice area trends. *Geophys. Res. Lett.* **40**(16), 4328–4332 (2013).

17. Pauling, A. G., Bitz, C. M., Smith, I. J. & Langhorne, P. J. The response of the Southern Ocean and Antarctic sea ice to freshwater from ice shelves in an Earth System Model. *J. Clim.* **29**(5), 1655–1672 (2016).

18. Bronselaer, B. et al. Change in future climate due to Antarctic meltwater. *Nature* **564**(7734), 53–58 (2018).

19. Park, W. & Latif, M. Ensemble global warming simulations with idealized Antarctic meltwater input. *Clim. Dynam.* **52**(5-6), 3223–3239 (2019).

20. Schloesser, F. et al. Antarctic iceberg impacts on future Southern Hemisphere climate. *Nat. Clim. Change* **9**(9), 672–677 (2019).

21. Rye, C. D. et al. Antarctic glacial melt as a driver of recent Southern Ocean climate trends. *Geophys. Res. Lett.* **47**(11), e2019GL086892 (2020).

22. Goosse, H., Lefebvre, W., de Montety, A., Crespin, E. & Orsi, A. H. Consistent past half-century trends in the atmosphere, the sea ice and the ocean at high southern latitudes. *Clim. Dynam.* **33**(7–8), 999–1016 (2009).

23. Polvani, L. M., Waugh, D. W., Correa, G. J. P. & Son, S. W. Stratospheric ozone depletion: The main driver of twentieth-century atmospheric circulation changes in the Southern Hemisphere. *J. Clim.* **24**(3), 795–812 (2011).

24. Thompson, D. W. J., Solomon, S., Kushner, P. J., England, M. H., Grise, K. M. & Karoly, D. J. Signatures of the Antarctic ozone hole in Southern Hemisphere surface climate change. *Nat. Geosci.* **4**(11), 741–749 (2011).

25. Kostov, Y. et al. Fast and slow responses of Southern Ocean sea surface temperature to SAM in coupled climate models. *Clim. Dynam.* **48**(5-6), 1595–1609 (2017).

26. Blanchard-Wrigglesworth, E., Roach, L. A., Donohoe, A. & Ding, Q. Impact of winds and Southern Ocean SSTs on Antarctic sea ice trends and variability. *J. Clim.* **34**(3), 949–965 (2021).
27. Zhang, X., Deser, C. & Sun, L. Is there a tropical response to recent observed Southern Ocean cooling? *Geophys. Res. Lett.* **48**(5), e2020GL091235 (2021).
28. Rosenblum, E. & Eisenman, I. Sea ice trends in climate models only accurate in runs with biased global warming. *J. Clim.* **30**(16), 6265–6278 (2017).
29. Sun, S. & Eisenman, I. Observed Antarctic sea ice expansion reproduced in a climate model after correcting biases in sea ice drift velocity. *Nat. Commun.* **12**, 1060 (2021).
30. Polvani, L. M. & Smith, K. L. Can natural variability explain observed Antarctic sea ice trends? New modeling evidence from CMIP5. *Geophys. Res. Lett.* **40**(12), 3195–3199 (2013).
31. Zunz, V., Goosse, H. & Massonnet, F. How does internal variability influence the ability of CMIP5 models to reproduce the recent trend in Southern Ocean sea ice extent? *Cryosphere* **7**(2), 451–468 (2013).
32. Ding, Q., Steig, E. J., Battisti, D. S. & Küttel, M. Winter warming in West Antarctica caused by central tropical Pacific warming. *Nat. Geosci.* **4**(6), 398–403 (2011).
33. Li, X., Holland, D. M., Gerber, E. P. & Yoo, C. Impacts of the north and tropical Atlantic Ocean on the Antarctic Peninsula and sea ice. *Nature* **505**(7484), 538–542 (2014).
34. Simpkins, G. R., McGregor, S., Taschetto, A. S., Ciasto, L. M. & England, M. H. Tropical connections to climatic change in the extratropical Southern Hemisphere: The role of Atlantic SST trends. *J. Clim.* **27**(13), 4923–4936 (2014).

35. Schneider, D. P., Deser, C. & Fan, T. Comparing the impacts of tropical SST variability and polar stratospheric ozone loss on the Southern Ocean westerly winds. *J. Clim.* **28**(23), 9350–9372 (2015).
36. Meehl, G. A., Arblaster, J. M., Bitz, C. M., Chung, C. T. Y. & Teng, H. Antarctic sea-ice expansion between 2000 and 2014 driven by tropical Pacific decadal climate variability. *Nat. Geosci.* **9**(8), 590–595 (2016).
37. Purich, A. et al. Tropical Pacific SST drivers of recent Antarctic sea ice trends. *J. Clim.* **29**(24), 8931–8948 (2016).
38. Clem, K. R., Fogt, R. L., Turner, J., Lintner, B. R., Marshall, G. J., Miller, J. R. & Renwick, J. A. Record warming at the South Pole during the past three decades. *Nat. Clim. Change* **10**(8), 762–770 (2020).
39. Li, X., Holland, D. M., Gerber, E. P. & Yoo, C. Rossby waves mediate impacts of tropical oceans on west Antarctic atmospheric circulation in austral winter. *J. Clim.* **28**(20), 8151–8164 (2015).
40. Wang, G. et al. Compounding tropical and stratospheric forcing of the record low Antarctic sea-ice in 2016. *Nat. Commun.* **10**, 13 (2019).
41. Stuecker, M. F., Bitz, C. M. & Armour, K. C. Conditions leading to the unprecedented low Antarctic sea ice extent during the 2016 austral spring season. *Geophys. Res. Lett.* **44**(17), 9008–9019 (2017).
42. Meehl, G. A. et al. Sustained ocean changes contributed to sudden Antarctic sea ice retreat in late 2016. *Nat. Commun.* **10**, 14 (2019).
43. Eayrs, C., Li, X., Raphael, M. N. & Holland, D. M. Rapid decline in Antarctic sea ice in recent years hints at future change. *Nat. Geosci.* **14**(7), 460–464 (2021).
44. Sigmond, M. & Fyfe, J. C. Has the ozone hole contributed to increased Antarctic sea ice extent? *Geophys. Res. Lett.* **37**(18), L18502 (2010).

45. Bitz, C. M. & Polvani, L. M. Antarctic climate response to stratospheric ozone depletion in a fine resolution ocean climate model. *Geophys. Res. Lett.* **39**(20), L20705 (2012).

46. Ferreira, D., Marshall, J., Bitz, C. M., Solomon, S. & Plumb, A. Antarctic ocean and sea ice response to ozone depletion: a two-time-scale problem. *J. Clim.* **28**(3), 1206–1226 (2015).

47. Seviour, W. J. M. et al. The Southern Ocean sea surface temperature response to ozone depletion: a multimodel comparison. *J. Clim.* **32**(16), 5107–5121 (2019).

48. Holland, P. R. & Kwok, R. Wind-driven trends in Antarctic sea-ice drift. *Nat. Geosci.* **5**(12), 872–875 (2012).

49. Chung, E.-S., Timmermann, A., Soden, B. J., Ha, K.-J., Shi, L. & John, V. O. Reconciling opposing Walker circulation trends in observations and model projections. *Nat. Clim. Change* **9**(5), 405–412 (2019).

50. Kosaka, Y. & Xie, S.-P. Recent global-warming hiatus tied to equatorial Pacific surface cooling. *Nature* **501**, 403–407 (2013).

51. Li, X. et al. Tropical teleconnection impacts on Antarctic climate changes. *Nat. Rev. Earth Environ.* **2**, 680–698 (2021).

52. Handcock, M. S. & Raphael, M. N. Modeling the annual cycle of daily Antarctic sea ice extent. *Cryosphere* **14**(7), 2159-2172 (2020).

53. Chung, E.-S. & Soden, B. J. Hemispheric climate shifts driven by anthropogenic aerosol-cloud interactions. *Nat. Geosci.* **10**(8), 566–571 (2017).

54. Lee, S.-K., Volkov, D. L., Lopez, H., Cheon, W. G., Gordon, A. L., Liu, Y. & Wanninkhof, R. Wind-driven ocean dynamics impact on the contrasting sea-ice trends around West Antarctica. *J. Geophys. Res. Oceans* **122**(5), 4413–4430 (2017).

409

Methods

Observational Datasets and Model Simulation Output

The National Snow and Ice Data Center (NSIDC) Sea Ice Index data (version 3, data set id: G02135) derived from Nimbus-7 SMMR and DMSP SSM/I-SSMIS passive microwave brightness temperatures[55] are used to analyze observed changes in Antarctic sea ice extent (SIE), defined as the total area of pixels with sea ice concentration greater than 15%. The NSIDC G02135 SIE data are available beginning in November 1978. To examine SIE changes prior to the period of continuous satellite monitoring, we also used the NSIDC ESMR-SSMR-SSMI-merged SIE data set (data set id: NSIDC-0192)[56] over the period 1973–2002, NOAA/NMC/CAC Arctic and Antarctic Monthly Sea Ice Extent digitized from weekly operational sea ice charts (version 1, data set id: G00917)[57] over the period 1973–1990, and SIE for September 1964 from the Nimbus-1 satellite (19.7×10^6 km^2)[58]. According to ref. 58, the uncertainty range of Nimbus-1 SIE for September 1964 is from 18.9 to 20.4×10^6 km^2, implying that the SIE in 1964 was larger than in any September measurements since 1979 except for 2013 and 2014. As these products are not intercalibrated, for NSIDC-0192 and G00917, the mean bias is computed for each calendar month over the respective overlapping period with NSIDC G02135 and then removed. In the case of the Nimbus-1 SIE for September 1964, potential biases were not adjusted because there is no overlapping period with other products. Although the mean bias may not be constant in time over the overlapping period, the pre-1979 SIE variability shown in Fig. 1c is consistent with previous studies[59–61]. In addition to these NSIDC products, sea ice concentrations from the Hadley Centre Sea Ice and Sea Surface Temperature (HadISST) data set[62] are used to determine the spatial pattern of the sea ice concentration trend.

Based on the close relationship between SIE and SST changes in the Southern Ocean[3,4,6], we also examined multi-decadal variability in Southern Ocean (SO, south of 50ºS) SSTs. To account for observational uncertainties due to insufficient in-situ measurements in the SO prior to the 1980s[3], we use multiple reconstructed/reanalysis data sets: NOAA's Extended Reconstructed Sea Surface Temperature version 5 (ERSSTv5)[63] over the period 1950–2020, HadISST[62] over the period 1950–2020, Centennial in situ Observation-Based Estimates (COBE) SST2[64] over the period 1950–2019, and the European Centre for Medium-Range Weather Forecasts (ECMWF) Reanalysis v5 (ERA5)[65] over the period 1950–2020. Despite potential SST uncertainties over the pre-satellite period, the SST variability is broadly consistent with other independent in-situ observations[3]. In addition, although there is large spread in SO SSTs among the reconstructed/reanalysis datasets (Figs. 1d and 4a), as shown in Supplementary Fig. 1, the spread decreases substantially if the SST variability is determined using only datasets (i.e., ERSST and ERA5) that are consistent with a quality-checked, bias-adjusted non-interpolated dataset (i.e., HadSST4[66]). To represent the time evolution of the global-mean, annual-mean surface temperature, we use the average of four data sets: HadCRUT5.0.1.0[67], GISTEMPv4[68,69], Berkeley Earth[70], and NOAA globaltemp v5.0.0[71]. These observational datasets are listed in Supplementary Table 1.

The observation-based changes in SIE, SSTs and global-mean temperature are compared to simulated changes from multiple initial-condition Large Ensembles conducted with Earth system models under historical forcing (and RCP8.5 forcing over the period 2006–2014 for some models), in which ensemble members are forced by the same external forcing but with slightly different initial conditions. Since the imposed external forcing is identical across ensemble members of a given model, the ensemble-mean change can be regarded as a forced response to the imposed external forcing. To reduce uncertainties in the estimated forced response, Coupled Model Intercomparison Project (CMIP) phase 5 (CMIP5) and CMIP6-class models, that have more than 15 ensemble members over the period 1979–2014, are analyzed in this study: two CMIP5-class[72] models, i.e., CanESM2 Large Ensemble[73] and

Community Earth System Model (CESM) version 1 (CESM1) Large Ensemble[74], and seven CMIP6-class[75] models, i.e., ACCESS-ESM1-5, CanESM5 (with two physics options available), CESM2 Large Ensemble[76], EC-Earth3, IPSL-CM6A-LR, NorCPM1, and UKESM1-0-LL. The number of ensemble members and forcing information are given in Supplementary Table 2. As shown in Supplementary Fig. 2, the mean seasonal cycle of Antarctic total SIE over the period 1979–2014, characterized by the maximum around September and the minimum around February, is broadly consistent with that from NSIDC G02135, although some models, such as EC-Earth3, exhibit noticeable discrepancies in amplitude. We also examined the characteristics of unforced variability of sea ice and SSTs using pre-industrial control simulation output (Supplementary Table 2).

Previous studies have suggested that the Antarctic climate can be affected by climate variability in the Atlantic and Pacific via atmospheric teleconnections[32–38]. To further enhance our understanding of the potential linkage of sea ice and SST changes in the SO to Atlantic and Pacific climate variability, we analyzed coupled model simulation output from the idealized SST forcing experiments conducted as part of the CMIP6 Decadal Climate Prediction Project (DCPP)[77]. The DCPP SST forcing experiments analyzed in this study are designed to investigate the response of coupled models to the patterns of Atlantic Multidecadal Variability (AMV) and Interdecadal Pacific Oscillation (IPO) by restoring North Atlantic and Pacific SSTs, respectively, to both positive and negative anomaly patterns of AMV and IPO superimposed on model control-run climatology over a 10-year period. In addition to the AMV and IPO experiments, we analyzed output from pacemaker experiments in which the observed SST anomalies in the eastern equatorial Pacific were assimilated over the period 1950–2014. As the pacemaker experiments were forced with the same external forcings as the historical experiments, the deviations from the corresponding historical experiments largely represent changes due to unforced variability of the eastern equatorial

Pacific SSTs. More detailed information on these DCPP experiments can be found in ref. 77. We focus on simulation output for IPSL-CM6A-LR because sea ice fields are available for all of these DCPP experiments. The number of ensemble members is 25 for the AMV experiments, 10 for the IPO experiments, and 10 for the pacemaker experiments.

AMV and IPO

An SST-based AMV (also referred to as AMO) index, defined as low-pass filtered area-averaged North Atlantic (Eq-60°N, 80°W-0°E) SST anomalies, is computed using the ERSST version 5 data set. A positive AMV phase is characterized by positive SST anomalies over most of the North Atlantic Ocean. Instead of detrending the SST anomalies to remove the climate change signal, following ref. 78, we subtracted the global-mean values from corresponding SST anomalies at each grid point over the North Atlantic. This method is also applied to the pre-industrial control simulation SST fields from CMIP5 and CMIP6 models. Although ref. 78 devised this method to avoid errors inherent to the detrending method, the AMV index computed in this way is also likely to include errors as the externally forced change is not spatially uniform over the globe.

Based upon the close connection of AMV to the Atlantic Meridional Overturning Circulation, the AMV has been regarded as internally generated, unforced climate variability[79,80]. However, North Atlantic climate variability might be driven in part by changes in external forcing agents such as sulfate aerosols[81].

Following ref. 82, the IPO index is computed as the low-pass filtered difference between the SST anomaly averaged over the central-to-eastern equatorial Pacific (10ºS-10ºN, 170ºE-90ºW) and the average of the SST anomaly over the Northwest Pacific (25ºN-45ºN, 140ºE-145ºW) and the Southwest Pacific (50ºS-15ºS, 150ºE-160ºW). This method is applied to both the ERSST version 5 data set and CMIP5/CMIP6 pre-industrial control simulation SST fields.

A positive IPO phase is characterized by positive SST anomalies over the central-to-eastern equatorial Pacific and negative SST anomalies over the Northwest Pacific and Southwest Pacific.

To determine whether the observed AMV and IPO trends over the period 1979–2014 fall within the range simulated by climate models, histograms of model-simulated AMV and IPO trends over overlapping 36-year periods are computed using pre-industrial control runs. A comparison indicates that although the observed trends over the period 1979–2014 lie within the range simulated by climate models, they are unlikely to occur frequently (Supplementary Fig. 3). This implies that even if multi-decadal variability linked to the IPO and/or AMV is accurately represented in climate models, the observed sea ice and SST changes in the SO might not be captured by model simulations under historical forcing.

SST Trends Congruent with Observed Trends in the IPO and AMV

SST trends, which are congruent to observed trends in the IPO and AMV, are computed over the period 1979–2014. First, multiple linear regressions are conducted at each grid point against both the IPO and AMV, with SST anomalies as the dependent variable over the period 1950–2020. The resulting regression coefficients for IPO and AMV are then, respectively, multiplied by the observed IPO and AMV trends over the period 1979–2014 with the sum of the multiplicative products representing the congruent trends. The regression coefficients derived from climate model simulations under pre-industrial control conditions are also used to compute the SST trends congruent to the observed IPO and AMV trends.

Statistical Information

We used the standard least squares linear regression approach to compute correlation coefficients, regression coefficients, and trends. Statistical significance of the computed correlation coefficients, regression coefficients and trends is determined using a two-sided Student's *t*-test at the 95% confidence level with reduced degrees of freedom to account for autocorrelation in a given time series. In the case of multi-model mean trends or ensemble-mean trends, the significance is determined by checking whether or not the multi-model mean or ensemble-mean trend exceeds two standard deviations of the trend across the models or the ensemble members. In Fig. 5, the significance of the response to a phase transition of AMV or IPO is determined using the Student's *t*-test at the 95% confidence level by comparing the ensemble-mean response in the positive phase SST pattern experiment relative to the corresponding control experiment and that for the counterpart experiment relative to the control experiment.

Data Availability

The NSIDC data are available at https://nsidc.org, the ERSST version 5 data set at https://psl.noaa.gov/data/gridded/data.noaa.ersst.v5.html, the HadISST data set at https://www.metoffice.gov.uk/hadobs/hadisst/data/download.html, the COBE SST2 data set at https://psl.noaa.gov/data/gridded/data.cobe2.html, the ERA5 data set at https://cds.climate.copernicus.eu, the HadSST4 data set at https://www.metoffice.gov.uk/hadobs/hadsst4/, the HadCRUT5.0.1.0 data set at https://www.metoffice.gov.uk/hadobs/hadcrut5/, GISTEMPv4 at https://data.giss.nasa.gov/gistemp/, NOAA globaltemp v5.0.0 at https://www.ncei.noaa.gov/products/land-based-station/noaa-global-temp, the Berkeley Earth data set at http://berkeleyearth.org/data/, the CanESM2 Large Ensemble output at http://crd-data-donnees-rdc.ec.gc.ca/CCCMA/products/CanSISE/output/CCCma/CanESM2/, the CESM1 Large Ensemble output at https://www.cesm.ucar.edu/projects/community-projects/LENS/, the CESM2 Large Ensemble output at https://www.cesm.ucar.edu/projects/community-projects/LENS2/data-sets.html, and the CMIP6 simulation output at https://esgf-node.llnl.gov/projects/cmip6/.

Code Availability

Codes used to generate the plots in this paper are available from the corresponding author on request.

References

55. Fetterer, F., Knowles, K., Meier, W. N., Savoie, M. & Windnagel, A. K. Sea Ice Index, Version 3. Sea ice extent. Boulder, Colorado USA. NSIDC: National Snow and Ice Data Center (2017). https://doi.org/10.7265/N5K072F8. Accessed March 22nd 2021.
56. Stroeve, J. & Meier, W. N. Sea Ice Trends and Climatologies from SMMR and SSM/I-SSMIS, Version 3. Sea ice index. Boulder, Colorado USA. NASA National Snow and Ice Data Center Distributed Active Archive Center (2018). https://doi.org/10.5067/IJ0T7HFHB9Y6. Accessed March 11th 2021.
57. Ropelewski, C. F. NOAA/NMC/CAC Arctic and Antarctic Monthly Sea Ice Extent, 1973-1990, Version 1. Sea ice extent. Boulder, Colorado USA. NSIDC: National Snow and Ice Data Center (1983, updated 1990). https://doi.org/10.7265/N5Z60KZ1. Accessed March 11th 2021.
58. Meier, W. N., Gallaher, D. & Campbell, G. G. New estimates of Arctic and Antarctic sea ice extent during September 1964 from recovered Nimbus 1 satellite imagery. *Cryosphere* **7**(2), 699–705 (2013).
59. Kukla, G. & Gavin, J. Summer ice and carbon dioxide. *Science* **214**(4520), 497–503 (1981).

60. Zwally, H. J., Parkinson, C. L. & Comiso, J. C. Variability of Antarctic sea ice and changes in carbon dioxide. *Science* **220**(4601), 1005–1012 (1983).

61. Curran, M. A. J. et al. Ice core evidence for Antarctic sea ice decline since the 1950s. *Science* **302**(5648), 1203–1206 (2003).

62. Rayner, N. A. et al. Global analyses of sea surface temperature, sea ice, and night marine air temperature since the late nineteenth century. *J. Geophys. Res.* **108**(D14), 4407 (2003).

63. Huang, B. et al. Extended Reconstructed Sea Surface Temperature, Version 5 (ERSSTv5): Upgrades, validations, and intercomparisons. *J. Clim.* **30**(20), 8179–8205 (2017).

64. Hirahara, S., Ishii, M. & Fukuda, Y. Centennial-scale sea surface temperature analysis and its uncertainty. *J. Clim.* **27**(1), 57–75 (2014).

65. Hersbach, H. et al. The ERA5 global reanalysis. *Q. J. R. Meteorol. Soc.* **146**(730), 1999–2049 (2020).

66. Kennedy, J. J., Rayner, N. A., Atkinson, C. P. & Killick, R. E. An ensemble data set of sea surface temperature change from 1850: The Met Office Hadley Centre HadSST.4.0.0.0 data set. *J. Geophys. Res. Atmos.* **124**(14), 7719–7763 (2019).

67. Morice, C. P., Kennedy, J. J., Rayner, N. A. & Jones, P. D. Quantifying uncertainties in global and regional temperature change using an ensemble of observational estimates: The HadCRUT4 data set. *J. Geophys. Res.* **117**, D08101 (2012).

68. GISTEMP Team. GISS Surface Temperature Analysis (GISTEMP), Version 4. https://data.nasa.gov/gistemp/ (2019).

69. Lenssen, N. J. L. et al. Improvements in the GISTEMP uncertainty model. *J. Geophys. Res. Atmos.* **124**(12), 6307–6326 (2019).

70. Rohde, R., Muller, R., Jacobsen, R., Perlmutter, S. & Mosher, S. Berkeley Earth temperature averaging process. *Geoinfor. Geostat.: An Overview 1:2* (2013).
71. Vose, R. S. et al. NOAA's merged land-ocean surface temperature analysis. *Bull. Am. Meteorol. Soc.* **93**(11), 1677−1685 (2012).
72. Taylor, K. E., Stouffer, R. J. & Meehl, G. A. An overview of CMIP5 and the experiment design. *Bull. Am. Meteorol. Soc.* **93**(4), 485−498 (2012).
73. Kirchmeier-Young, M. C., Zwiers, F. W., Gillett, N. P. & Cannon, A. J. Attributing extreme fire risk in Western Canada to human emissions. *Clim. Change* **144**(2), 365–379 (2017).
74. Kay, J. E. et al. The Community Earth System Model (CESM) Large Ensemble Project: A community resource for studying climate change in the presence of internal climate variability. *Bull. Am. Meteorol. Soc.* **96**(8), 1333−1349 (2015).
75. Eyring, V., Bony, S., Meehl, G. A., Senior, C. A., Stevens, B., Stouffer, R. J. & Taylor, K. E. Overview of the Coupled Model Intercomparison Project Phase 6 (CMIP6) experimental design and organization. *Geosci. Model Dev.* **9**, 1937–1958 (2016).
76. Rodgers, K. B. et al. Ubiquity of human-induced changes in climate variability. *Earth Syst. Dynam.* https://doi.org/10.5194/esd-2021-50, in press (2021).
77. Boer, G. J. et al. The Decadal Climate Prediction Project (DCPP) contribution to CMIP6. *Geosci. Model Dev.* **9**(10), 3751-3777 (2016)
78. Trenberth, K. E. & Shea, D. J. Atlantic hurricanes and natural variability in 2005. *Geophys. Res. Lett.* **33**(12), L12704 (2006).
79. Delworth, T. L. & Mann, M. E. Observed and simulated multidecadal variability in the Northern Hemisphere. *Clim. Dynam.* **16**(9), 661–676 (2000).

80. Lapointe, F. et al. Annually resolved Atlantic sea surface temperature variability over the past 2,900 y. *Proc. Natl Acad. Sci. USA* **117**(44), 27171–27178 (2020).

81. Booth, B. B. B., Dunstone, N. J., Halloran, P. R., Andrews, T. & Bellouin, N. Aerosols implicated as a prime driver of twentieth-century North Atlantic climate variability. *Nature* **484**(7393), 228–232 (2012).

82. Henley, B. J., Gergis, J., Karoly, D. J., Power, S., Kennedy, J. & Folland, C. K. A Tripole Index for the Interdecadal Pacific Oscillation. *Clim. Dynam.* **45**(11–12), 3077–3090 (2015).

Acknowledgements

We are grateful to the National Snow and Ice Data Center, the National Oceanic and Atmospheric Administration Physical Sciences Laboratory, the European Centre for Medium Range Weather Forecasts, the Met Office Hadley Centre, Japan Meteorological Agency, the GISTEMP Team, the National Centers for Environmental Information, Berkeley Earth, the National Center for Atmospheric Research, Environment and Climate Change Canada and modeling centers participating in CMIP6 for providing their respective data sets. E.-S.C. and S.-J.K. were supported by the project PE21030 of the Korea Polar Research Institute. A.T., K.-J.H., K.B.R., S.-S.L. and L.H. were supported by the Institute for Basic Science (IBS) under IBS-R028-D1. M.F.S. was supported by NOAA's Climate Program Office's Modeling, Analysis, Predictions, and Projections (MAPP) program grant NA20OAR4310445. This is IPRC publication X and SOEST contribution Y. The CESM2 Large Ensemble simulations were conducted on the IBS/ICCP supercomputer "*Aleph*" through a partnership between the ICCP in South Korea and the CESM Project at the National Center for Atmospheric Research (NCAR) in the US. We thank Nan Rosenbloom and Jim Edwards for their hard work regarding the CESM2 Large Ensemble simulations.

Author contributions

E.-S.C. and S.-J.K. designed the study. E-S.C. performed the analysis and produced figures. S.-J.K, A.T., K.-J.H., S.-K.L., M.F.S., K.B.R., S.-S.L. and L.H. provided feedback on the analyses, the interpretation of the results, and the figures. All authors contributed to the writing of the manuscript and the improvement of the manuscript.

Competing interests

The authors declare no competing interests.

Correspondence and requests for materials should be addressed to S.-J.K.

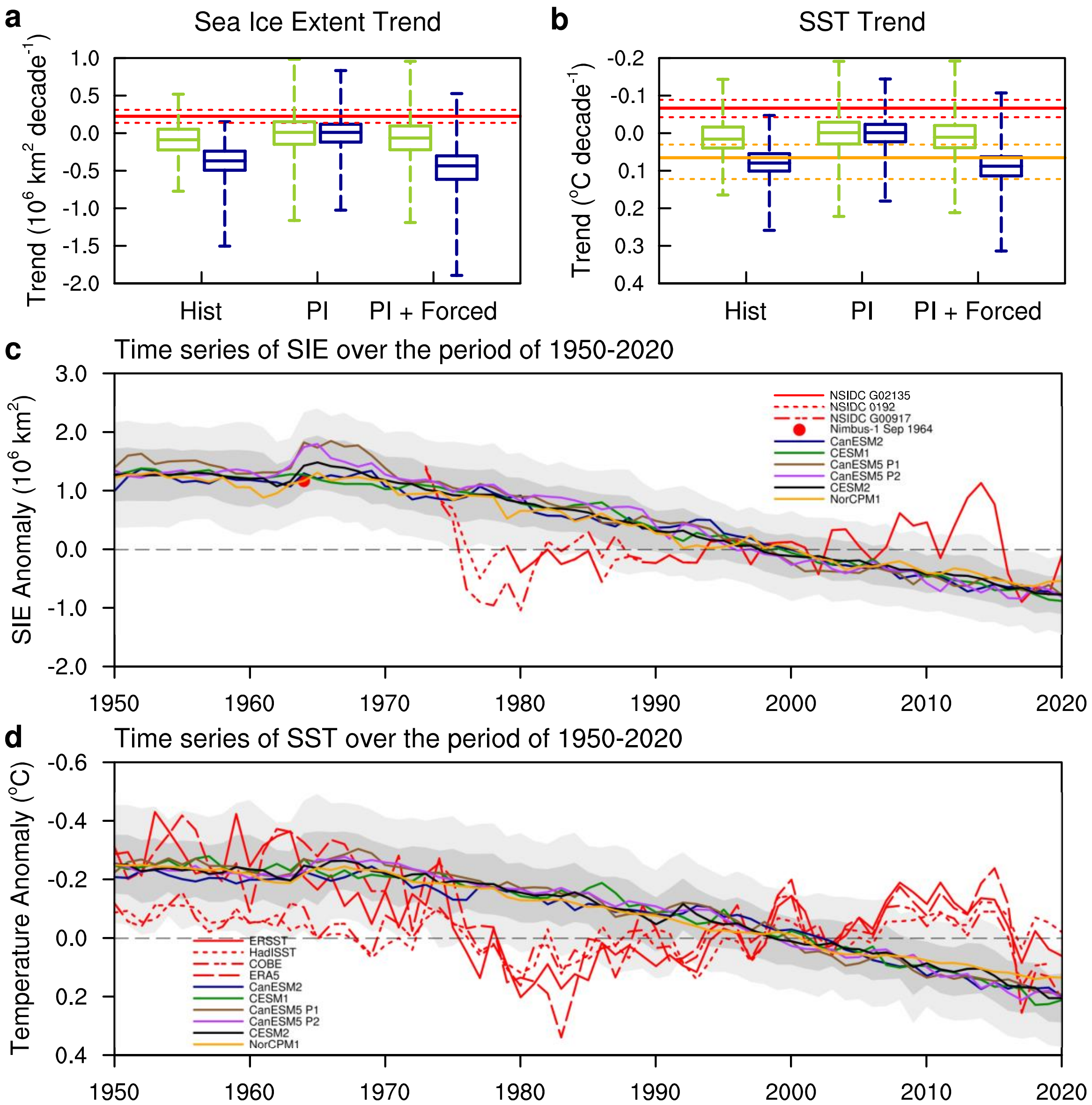

Fig. 1: Observed and model-simulated changes in annual-mean SIE and SST over the Southern Ocean (south of 50°S). **a**, Boxplots of model-simulated SIE trends over 29-year (yellow green) and 36-year (dark blue) periods for three cases: (Hist) trends over 1950–1978 and 1979–2014 under historical forcing, (PI) trends for all possible overlapping 29-year and 36-year segments of pre-industrial control runs, and (PI+Forced) PI trends with the corresponding ensemble-mean values for 1950–1978 and 1979–2014 added. The box covers the inter-quartile range with the line inside the box representing the median value across multi-ensemble models and whiskers denoting the maximum and minimum values. The red solid line denotes the satellite-observed 1979–2014 SIE trend with the accompanying dashed lines representing the standard error of the trend. **b**, Same as in **a**, but for SST trends. The orange solid line denotes the observed 1950–1978 SST trend averaged over four SST datasets

(ERSST, HadISST, COBE, and ERA5) with the accompanying dashed lines representing minimum and maximum trends. The solid and dashed lines in red denote the corresponding observed SST trends over 1979–2014. **c**, Timeseries of SIE anomaly relative to the 1979–2020 means. The red dot denotes the SIE anomaly for September 1964 from the Nimbus-1 satellite. For model simulations, lines denote the ensemble-mean anomaly for individual models. The shading indicates inter-ensemble variability for the CESM2 Large Ensemble with one and two standard deviations represented, respectively, by dark and light grey. **d**, Same as in **c**, but for SST anomaly. Note the reversed y-axis direction in **b** and **d**.

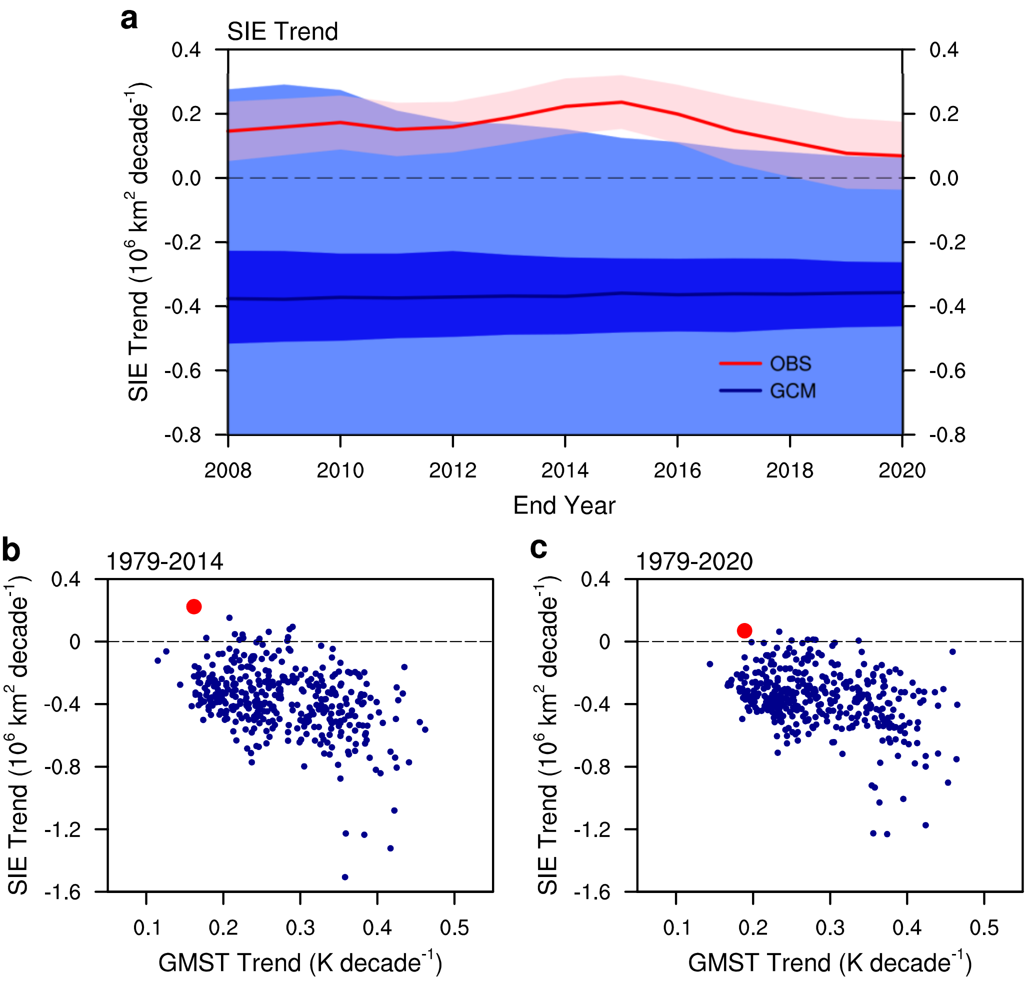

Fig. 2: Comparison of observed and model-simulated trends in Antarctic SIE and global-mean surface temperature. **a,** Timescale dependence of the model-observation discrepancy in the annual-mean Antarctic SIE trend. The abscissa denotes the end year of a given period starting in 1979. The solid line in red denotes the observed trend with the accompanying shading representing the standard error of the trend. The solid line in dark blue denotes the median values of model-simulated trends across multi-ensemble models with the corresponding inter-quartile and entire range represented, respectively, by dark and light shading. **b**, Scatter plot of annual-mean Antarctic SIE trend with the corresponding annual-mean global-mean surface temperature trend over 1979–2014. While the red dot denotes the observed trend, smaller dots in dark blue represent model-simulated trends. **c**, Same as in **b**, but for 1979–2020.

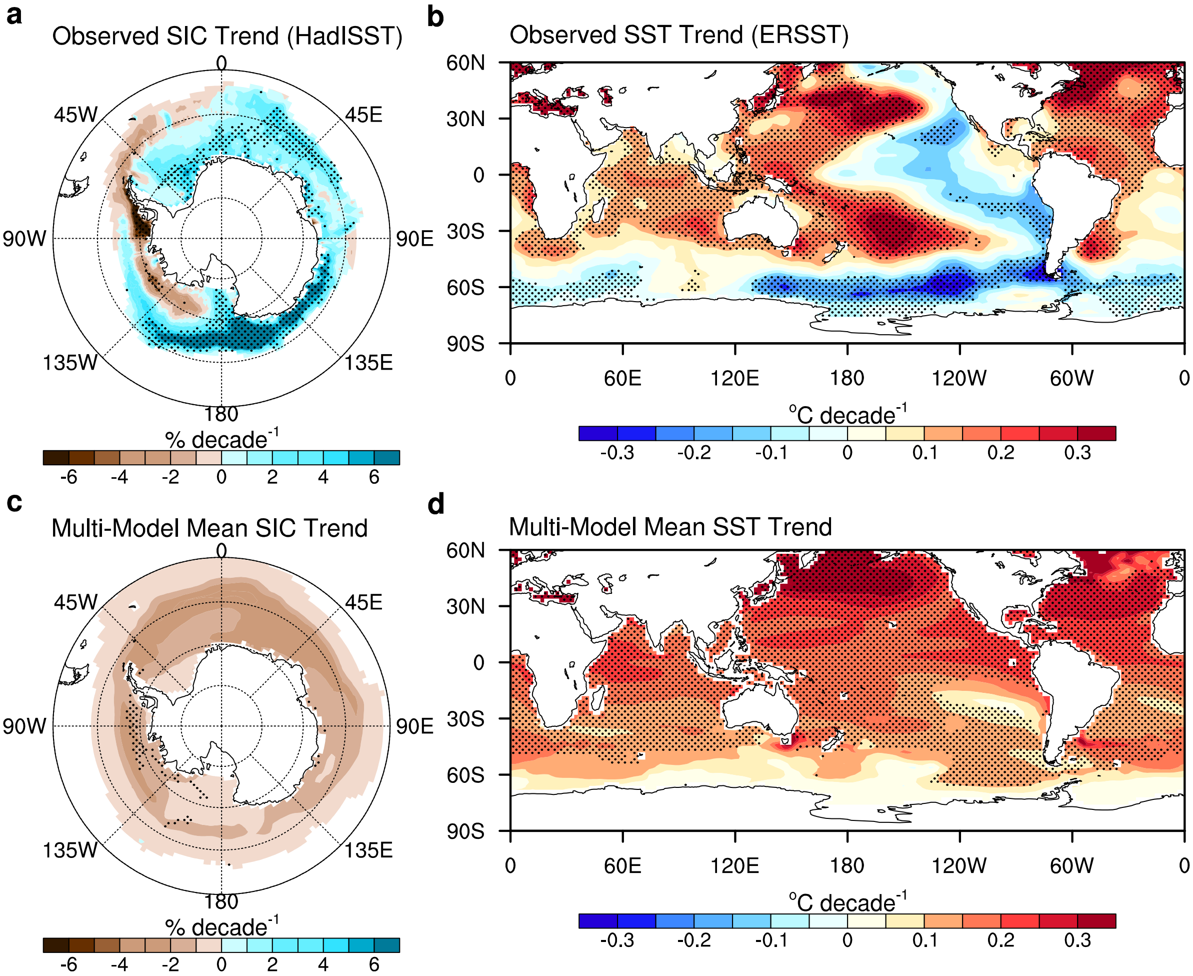

Fig. 3: Observed and model-simulated trends in annual-mean sea ice and SST over the period 1979–2014. **a**,**b**, Observed trends in sea ice concentration and SST: HadISST (**a**) and ERSST (**b**). **c**,**d**, Same as in **a** and **b**, but for multi-model mean of the ensemble-mean trends for a given model. For observations, stippling indicates statistical significance of the computed trends at the 95% confidence level. For the multi-model mean, stippling denotes regions where the multi-model mean exceeds two standard deviations of the trend across the models.

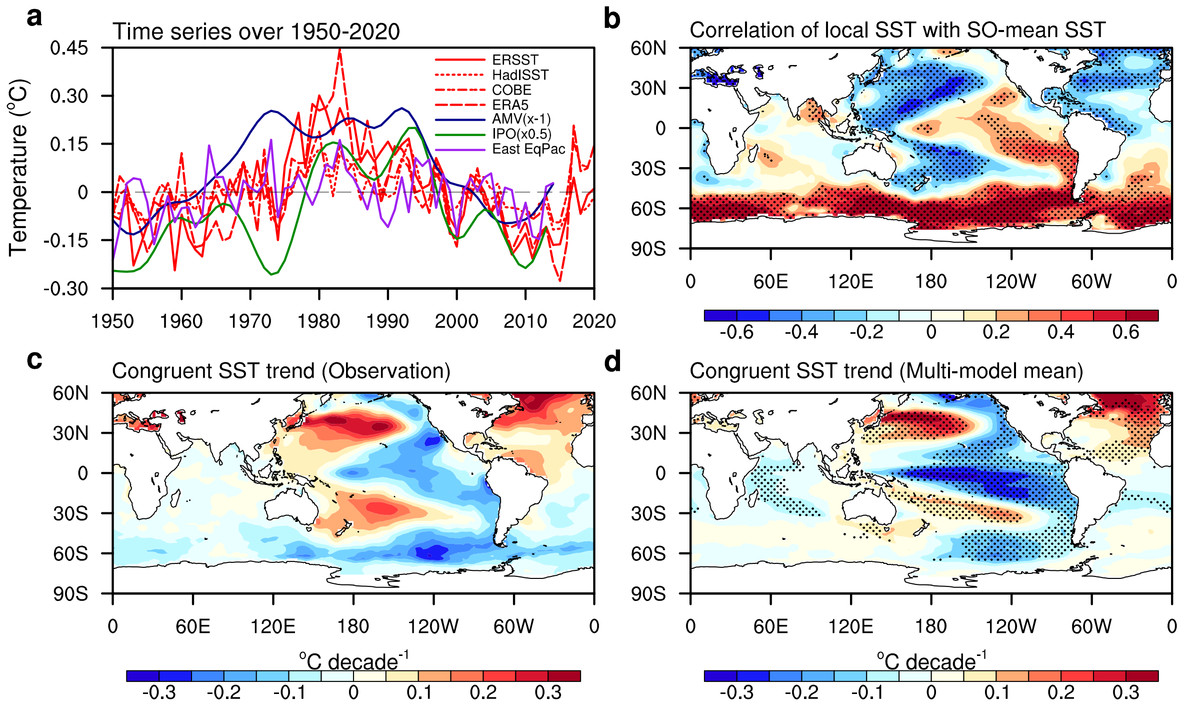

Fig. 4: Multidecadal variability of Southern Ocean SST and its connection to the AMV and IPO. **a**, Timeseries of detrended annual-mean Southern Ocean-mean SST changes over 1950–2020 (red lines). Also shown are timeseries of the AMV index (blue line with sign reversed), the IPO index (green, multiplied by 0.5), and model-simulated ensemble-mean Southern Ocean-mean SST changes resulting from observed SST variability in the eastern equatorial Pacific (purple). The model-simulated response to observed SST variability in the eastern equatorial Pacific is estimated by subtracting SST changes from coupled historical experiments with IPSL-CM6A-LR from those obtained from pacemaker experiments where the observed SST anomalies in the eastern equatorial Pacific were assimilated under the same forcing as in the historical experiments. **b**, Temporal correlation of detrended ERSST annual-mean SST change at each grid point with corresponding Southern Ocean-mean change. **c**, SST trends over 1979–2014, which are linearly congruent with the observed IPO and AMV trends over 1979–2014. The congruent trends are estimated by summing up the multiplicative product of the observed IPO trend and the regression coefficient for the IPO at each grid point in the multiple linear regression of detrended SST anomalies against the IPO and AMV indices and that for the AMV. **d**, Same as in **c**, but with the regression coefficients derived from multi-model pre-industrial control runs. Stippling indicates statistical significance of the correlation coefficients at the 95% confidence level in **b**, and regions where the multi-model mean trend exceeds two standard deviations of the trend across the models in **d**.

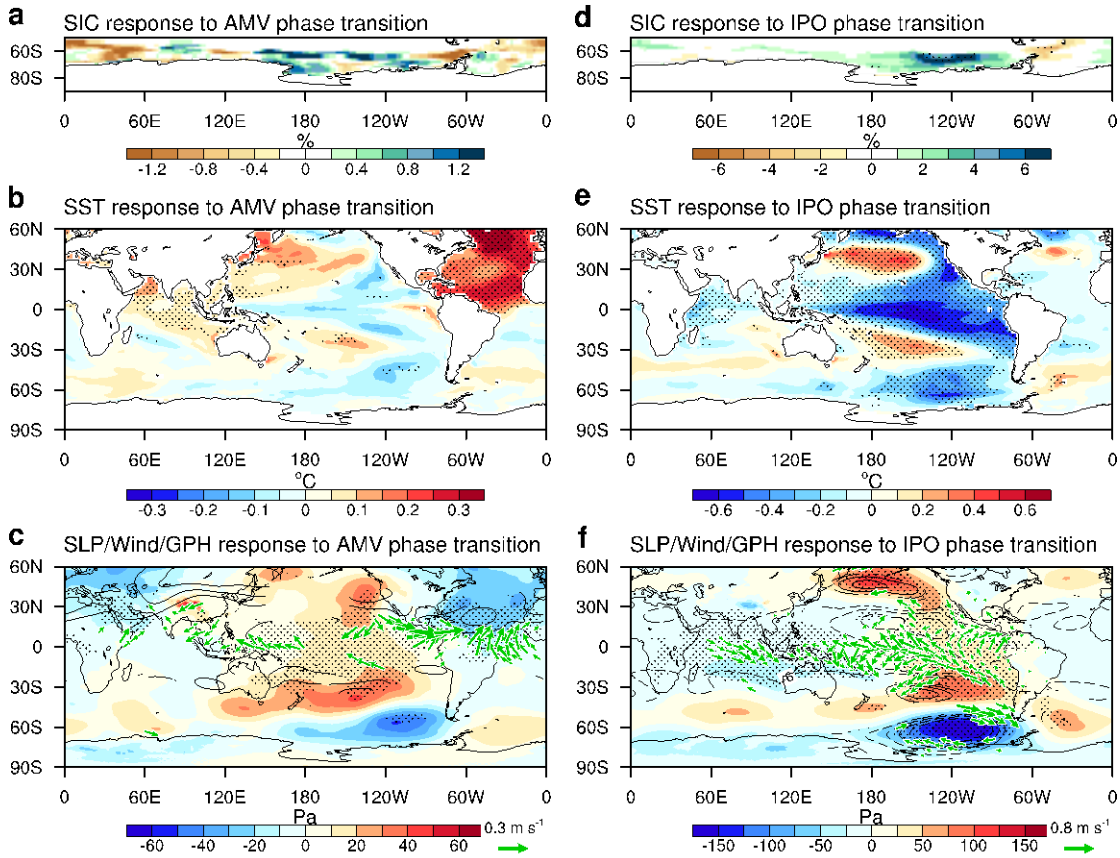

Fig. 5: Influence of internal variability in the Atlantic and Pacific on sea ice, SST, and circulation in coupled model simulations. **a**, Response of sea ice concentration to a negative-to-positive phase transition of the Atlantic Multidecadal Variability in idealized SST restoring experiments with IPSL-CM6A-LR. The response is computed by subtracting annual-mean sea ice concentration changes averaged over a 10-year period in the negative phase SST pattern experiment, in which North Atlantic SSTs are restored to negative AMV anomaly superimposed on model control-run climatology, relative to the corresponding control experiment, in which North Atlantic SSTs are restored to model control-run climatology, from that in the counterpart positive phase experiment. **b**, Same as in **a**, but for SST response. **c**, Same as in **a**, but for sea level pressure (shading), surface winds (vectors), and 300-hPa geopotential height (contours) responses. **d**-**f**, Same as in **a**-**c**, but for responses to a positive-to-negative phase transition of the Interdecadal Pacific Oscillation. In **a**-**f**, stippling denotes regions where the change is statistically significant at the 95% confidence level. In **c** and **f**, surface wind and 300-hPa geopotential height changes are shown over regions where the change is statistically significant at the 95% confidence level.